Supplemental text and figures for

Coupled hydrogen and fluorine incorporation in garnet: new constraints from FTIR, ERDA, SIMS, and EPMA

Jed L. Mosenfelder, Anette von der Handt, Anthony C. Withers, Hélène Bureau, Caroline Raepsaet, and George R. Rossman

1. Additional sample details

Sample localities are listed in Table 1 for all of the grossular garnets used in this study. The geologic context of these samples is discussed in more detail in Section 7. GRR42, GRR229, GRR771, GRR1122, and GRR1429 were previously characterized by FTIR and EPMA (Rossman and Aines 1991). The H content of GRR732 was measured using continuous flow mass spectrometry (O'Leary et al. 2007). GRR1386 was studied using Fourier transform infrared spectroscopy (FTIR) and nuclear magnetic resonance (NMR) by Cho and Rossman (1993), but GRR1386a is a different single crystal derived from the same collection of stream gravel. Crystals from this collection have similarly shaped IR spectra but vary significantly in color, H content, and minor element chemistry (chiefly V and Fe concentrations). Figure OM1 is a comparison of FTIR spectra for all of the East African grossular garnets used in this study.

JLM83a is an orange grossular garnet from the electron microprobe standard collection at UMN. Garnets from this locality (Asbestos, Quebec, Canada) – noted for their optical birefringence – have been investigated using FTIR (Rossman and Aines 1986; Allen and Buseck 1988; Rossman and Aines 1991) and nuclear reaction analysis (NRA; Rossman and Aines 1991).

During the 2012 SIMS session, we collected data on a variety of pyrope, spessartine, and andradite garnets in addition to the grossular samples focused on in this paper. SIMS data are discussed in the main text for 11 spessartine and two andradite-rich garnets. FTIR spectra of

some of these garnets referred to in the main text are displayed in Figures OM2 and OM3, respectively. Nine of the spessartine garnets were collected from the Rutherford Mine, near the town of Amelia, Virginia, U.S.A. Seven of these samples (R2G1, R2G3, R2G5, R2G6, R2G7, R2G8, and R2G9) were selected from the study of Arredondo et al. (2001) and one (GRR44-1B; Fig. OM2) was studied using FTIR and NRA by Rossman et al. (1988). The IR spectrum of one additional Rutherford Mine spessartine (GRR43) has been presented previously (Amthauer and Rossman, 1998). The other two spessartine garnets (Fig. OM2) come from a pegmatite in the Ramona district in California, U.S.A. (GRR42; Rossman et al., 1988) and from Mozambique (GRR875). One andradite-rich ($Grs_{26}Adr_{74}$) garnet (GRR1830; Fig. OM3) was collected from Redwood Canyon, Tulare Country, CA, USA; it formed via contact metamorphism of calcareous rocks in a roof pendant (Jenkins, 1943). The other andradite (GRR2103; Fig. OM3) is a demantoid from the Klodovka Mine (north of Ekaterinburg, Ural Mountains, Russia).

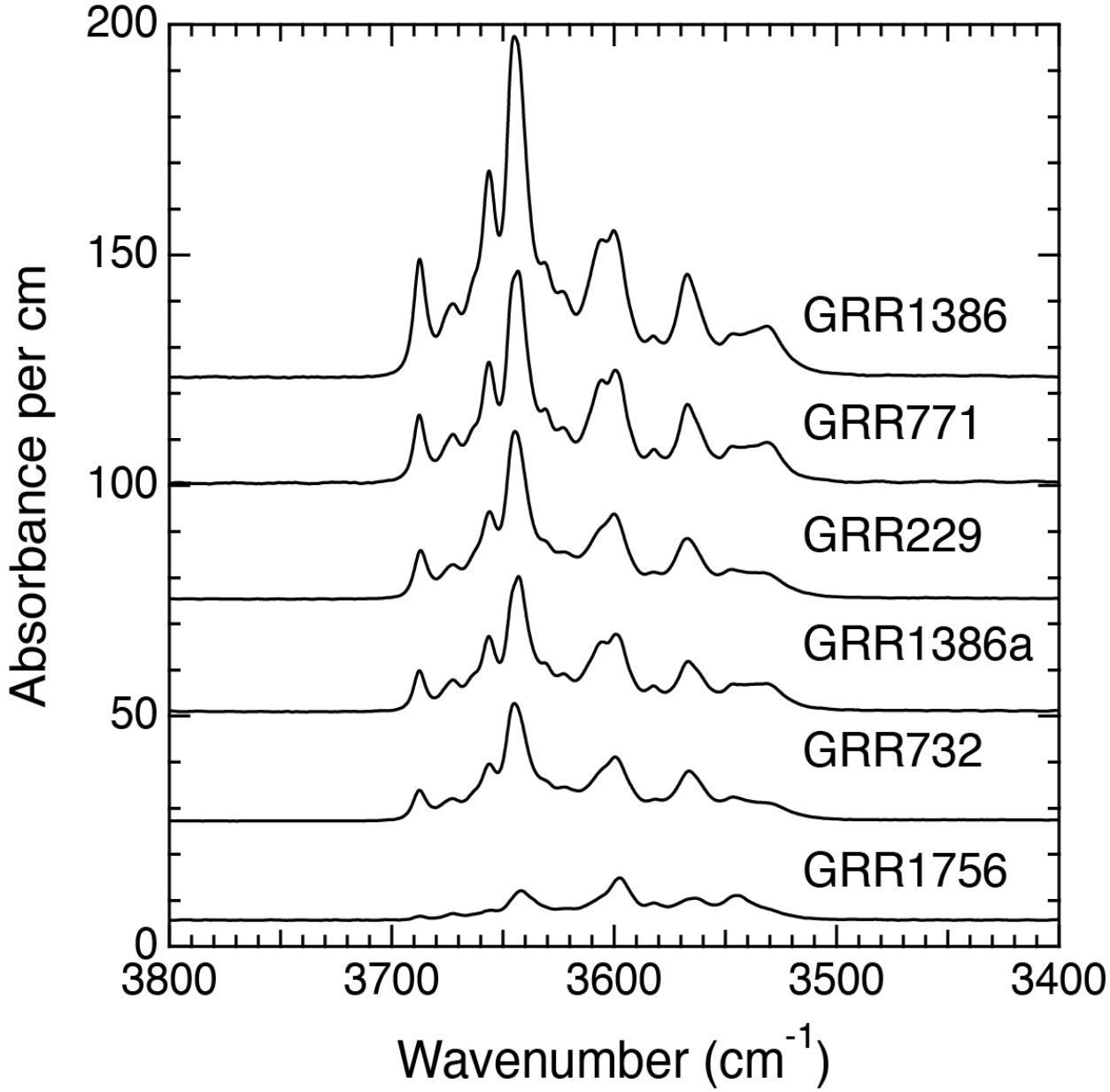

FIGURE OM1. FTIR spectra of East African grossular garnets, plotted in order of increasing H_2O and F content from bottom to top. GRR1756 (class 7) is similar to the other East African garnets (class 2b) with the exception of a stronger peak at 3599 cm^{-1} compared to the peak 3647 cm^{-1}. All spectra are normalized to 1 cm thickness, plotted without baseline correction, and arbitrarily offset from each other for clarity.

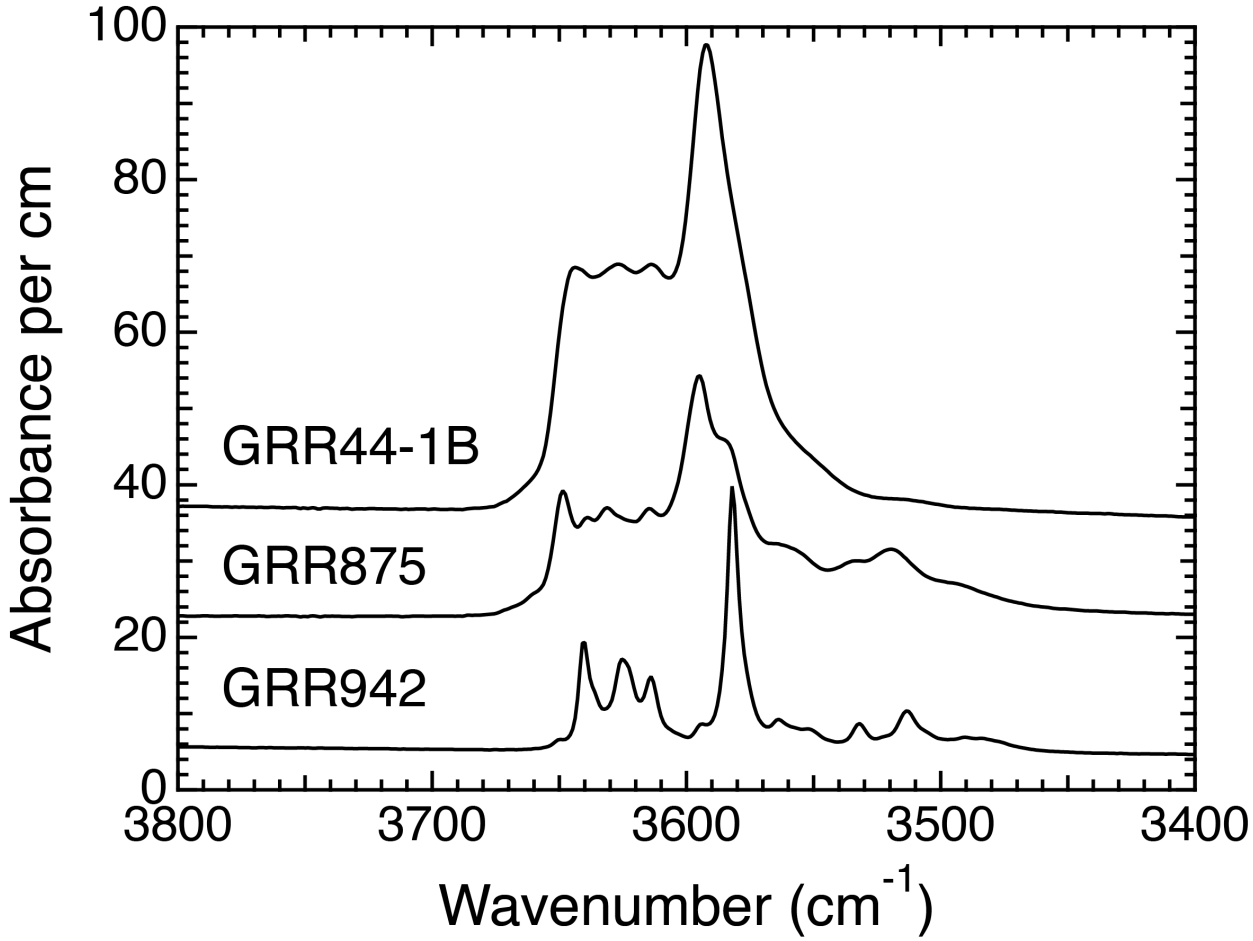

FIGURE OM2. FTIR spectra of spessartine GRR44-1B (Rutherford 2 Mine, Virginia, USA), GRR875 (Mozambique), and GRR942 (Ramona pegmatite, California, USA). Spectra are plotted without baseline correction and offset from each other for clarity.

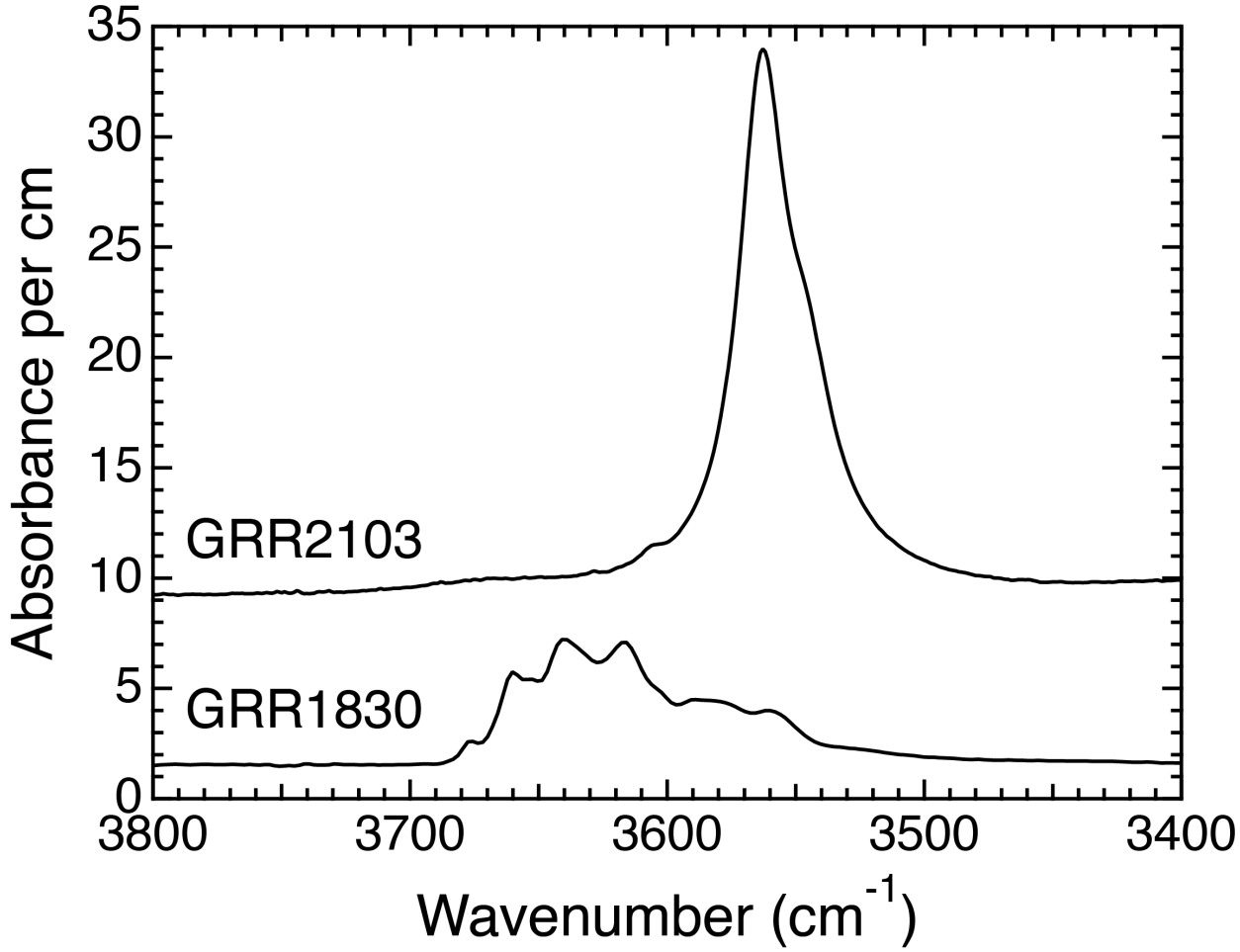

FIGURE OM3. FTIR spectra of andradite-rich garnets GRR2103 (Klodovka Mine, Ural Mountains, Russia) and GRR1830 (Redwood Canyon, California, USA). Spectra are plotted without baseline correction and offset from each other for clarity.

2. "Blank" reference materials and vacuum conditions

SIMS data ($^{16}O^{1}H/^{18}O$, $^{16}O^{1}H/^{30}Si$, $^{19}F/^{18}O$, and $^{19}F/^{30}Si$ ratios) were blank corrected using $^{16}O^{1}H$ and ^{19}F backgrounds monitored by analyzing "blank" reference materials: synthetic forsterite GRR1017 (characterized by Mosenfelder et al. 2011), a natural Cr-rich pyrope from Ugelvik, Norway (GRR332), and laboratory-dehydrated grossular (GRR1122-HT) and spessartine (GRR2215-HT).

For GRR332 we took care to prepare a section that was optically free of near-surface inclusions, such as the pyroxenes representing exsolution of a majoritic component that van Roermund et al. (2000) documented in garnets from this locality. FTIR spectra (Fig. OM4) reveal no OH above the detection limit (~1 μg/g H_2O) in GRR322. GRR332 is also presumed to be nominally F-free, based on comparison of its $^{19}F/^{18}O$ ratio to that of GRR1017.

GRR1122-HT was made by dehydrating GRR1122 at 1 atm and 1000 °C in a series of annealing steps, with FTIR spectra taken before and after each anneal (Fig. OM4). The first two anneals, lasting 72 hours each, were performed in a CO-CO_2 atmosphere in a Deltech gas-mixing furnace at f_{O_2} corresponding to approximately one order of magnitude below the quartz-fayalite-magnetite buffer (ΔQFM-1). Peak heights in the O-H stretching region significantly decreased after the first step but remained nearly constant after the second annealing. Therefore, we performed a final anneal in air in a muffle furnace, for 217 hours. After this anneal, sharp O-H peaks were no longer observed. GRR1122-HT gives consistently low ^{16}OH counts but high ^{19}F counts, indicating that the sample retained most of its fluorine during dehydration. Accordingly, it was used only for blank correction of $^{16}OH/^{30}Si$ and $^{16}OH/^{18}O$ ratios, whereas the fluorine data were corrected using either GRR332 or GRR1017. GRR2215-HT was made in the same way as

GRR1122-HT, with only one step at 1000 °C needed to fully dehydrate the starting material (GRR2215 spessartine, from the Shigar Valley in Pakistan).

Ultra-low vacuum conditions are critical for measuring trace concentrations of H and F in nominally anhydrous minerals using SIMS (e.g., Koga et al. 2003; Aubaud et al. 2007; Mosenfelder et al. 2011). Vacuum pressure in the SIMS sample chamber was higher in 2016 compared to 2012, despite using the same protocol in both sessions to achieve ultra-low vacuum (baking of the instrument prior to analysis and use of a liquid N_2 cold trap). The vacuum in the first session remained constant between 3.2×10^{-8} and 3.9×10^{-8} Pa, resulting in low blanks for ^{12}C, $^{16}O^{1}H$, and ^{19}F. In 2016, the vacuum started at 5.2×10^{-8} Pa and the blanks were higher (Table 3). Moreover, most of the analyses were collected in automated mode (Mosenfelder et al., 2011) overnight and the cold trap ran out of liquid N_2 towards the end of the automation. This event led to an order of magnitude increase in vacuum pressure and a spike in background ^{12}C, $^{16}O^{1}H$, and ^{19}F that adversely affected some analyses of JLM83a, as discussed in the results section of the main text.

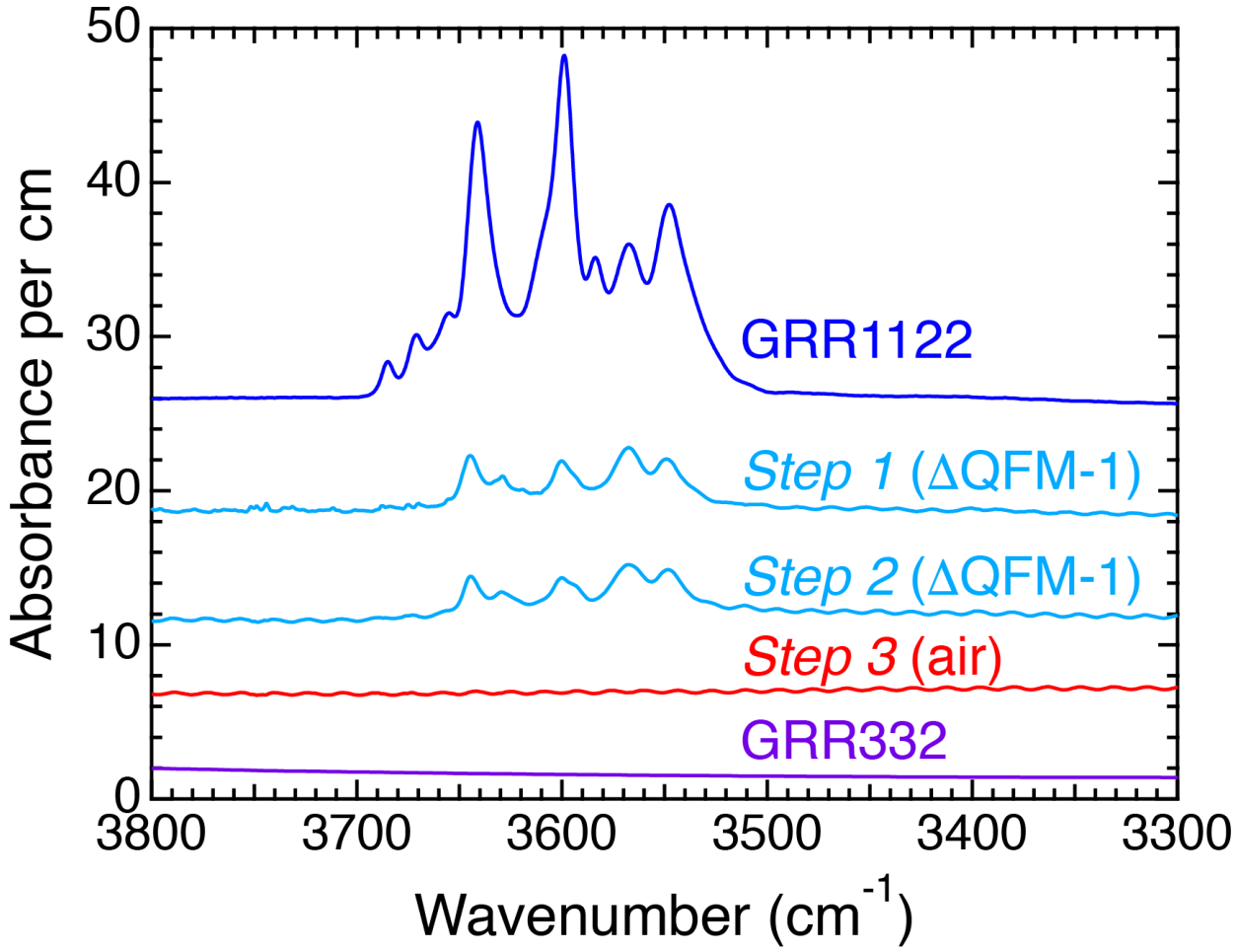

FIGURE OM4. FTIR spectra of grossular GRR1122, before and after three successive dehydration steps. Spectrum of pyrope GRR332 also displayed for comparison. Dehydration steps 1 and 2 were each conducted for 72 hours at 1000 °C and f_{O_2} near ΔQFM-1. Step 3 was performed for 217 hours in air at 1000 °C. After step 3, no sharp peaks are observable in the sample (see text and supplemental information for more discussion). Spectra are normalized to 1 cm thickness, plotted without baseline correction or any attempt to remove interference fringes, and offset from each other for clarity.

3. FTIR spectra: baseline correction and curve fitting

Appendix Table OM1 (separate excel file) contains FTIR spectral data with baseline corrections for all the grossular garnets. Baseline corrections were performed using OMNIC, OPUS, or Igor Pro software. For spectra collected at Caltech we corrected the baseline by applying cubic spline fits with manually chosen points to account for artifacts such as interference fringes, which we found difficult to subtract accurately by modeling. Spectra collected at UMN on JLM83a were corrected using a linear fit to the baseline between 3750 and 3300 cm^{-1}. The JLM83a spectra are mainly used to assess relative differences in a qualitative manner and were not corrected for the effects of convergence of the impinging IR beam, an inherent problem for thick samples (0.039 cm in this case) measured using IR microscopes with Cassegrainian objectives (Maldener et al. 2003).

After baseline correction, we calculated total integrated band areas (Abs_{tot}, considered here as absorbance/cm^2 in one direction, rather than multiplying one measurement by three as in some studies on garnets) over the wavenumber range from 3750 to 3000 cm^{-1} (Table 1). Some exceptions in this range were taken to account for noise on the baseline; the fits and wavenumber range for integration for each spectrum are provided in the supplementary material. Uncertainties of 1-3% in Abs_{tot} were assessed individually and subjectively for each sample, using criteria similar to Mosenfelder et al. (2015). These uncertainties do not take into account possible contributions from liquid water or an Fe^{2+} absorption band that are discussed in the results section. Uncertainties in sample thickness were ignored because we have previously found that they are inconsequential when propagated, as the overall uncertainty is dominated by uncertainty in the baseline.

After baseline correction, spectra were curve fit using the Multipeak Fitting 2 package in Igor Pro. The example of curve fitting provided in Figure OM5 for GRR1386 is discussed in the main text. Table OM2 (separate excel file) contains calculated peak heights and areas from curve fitting for GRR1386 and other samples.

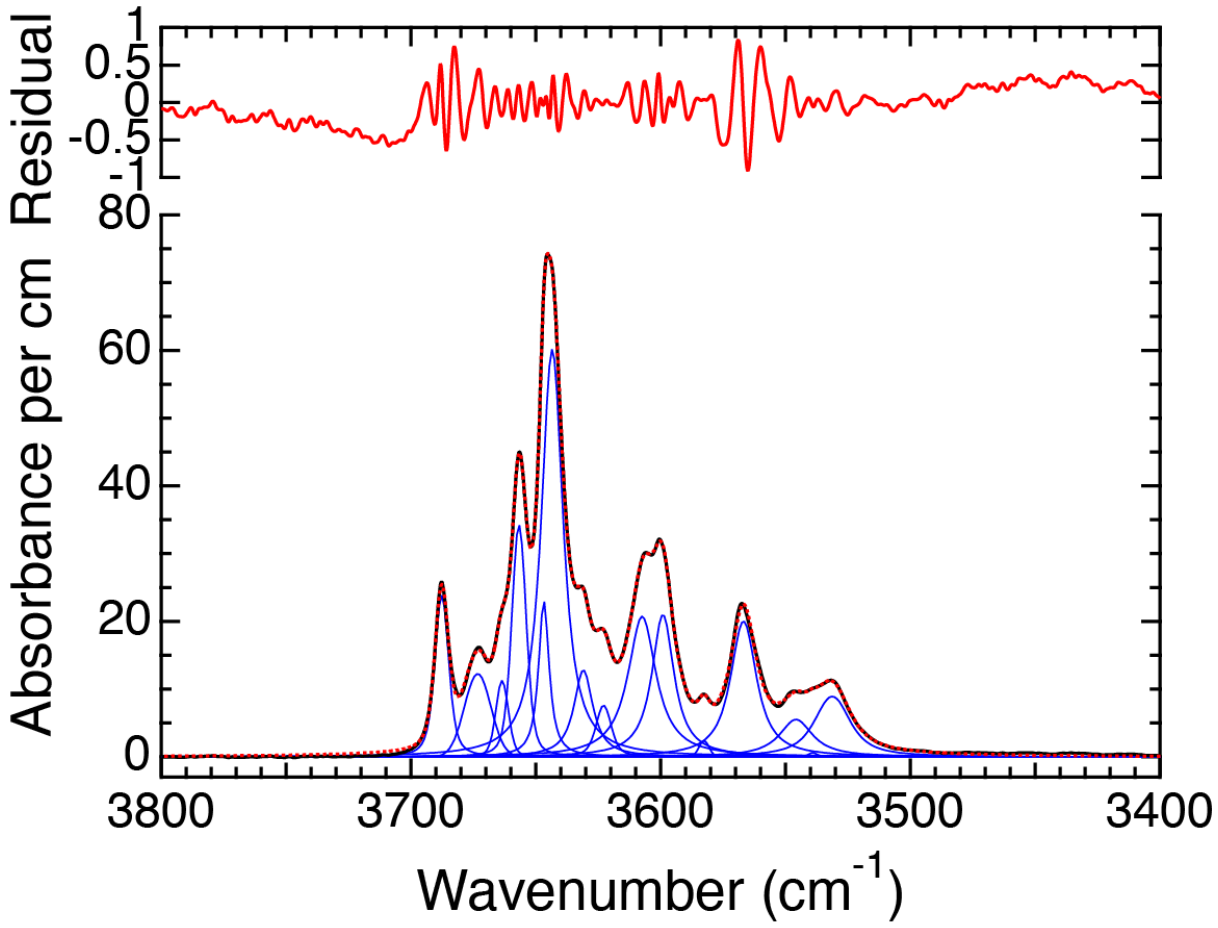

FIGURE OM5. Example of FTIR spectral curve fitting. Spectrum of GRR1386 (solid black curve) is overlain by the fit (dotted red curve), composed of 15 voigt peaks (solid blue curves; peak at 3539 cm^{-1} is not visible at this scale). Residuals are in the same units of absorbance (normalized to 1 cm) as the spectra.

4. ERDA

ERDA was performed at the Laboratoire d'Etudes des Eléments Légers, CEA, Saclay, France using a nuclear microprobe (Khodja et al. 2001) and improved methods for micro-ERDA

(Raepsaet et al. 2008, Bureau et al. 2009). The samples were mounted in indium and gold-coated prior to analysis. Analytical methods followed those outlined by Withers et al. (2012). We used a 3 MeV $^4He^+$ beam at 600 pA, focused to 3 μm x 3 μm. Analyses were conducted by rapidly scanning large areas, to prevent H loss. We used an analysis area for each sample of 386 x 200 μm and analysis durations between 3600 and 4830 s. Three detectors were simultaneously employed: an X-Ray detector to record particle induced X-Ray (PIXE) emissions, an annular detector to record Rutherford backscattered (RBS) particles, and an ERDA detector to record H atoms ejected from the sample through elastic collisions with the alpha particles. The sample holder was tilted in order to obtain a low grazing angle of 15° with respect to the sample surface, thus the beam size on the surface was enlarged to 12*3 μm^2. Well-known reference materials (Al_2O_3, FeS_2, SiO_2, $CaCO_3$, SnBi, Zr) were used to calibrate the RBS solid angle at 66.79 msr with a normal incidence (no tilt). The ERDA solid angle was calibrated at 16.34 msr in ERDA configuration (tilted) by using a Kapton standard assumed to be stoichiometric $C_{22}H_{10}O_5N_2$. The RBS spectrum provides quantification of the charge on the sample during the course of the ERDA measurement, therefore permitting H quantification. The elemental maps were first extracted for all detectors with RISMIN software (Daudin et al. 2003) to avoid any contaminated areas such as inclusions, grain boundaries, or cracks detected via RBS and PIXE mappings. Finally, SIMNRA software (Mayer 1999) was employed to obtain hydrogen concentrations that were converted to H_2O concentrations.

Simultaneously collected ERDA (H) and PIXE (Ca) maps of GRR771 (Fig. OM6) reveal an area with anomalously high H and low Ca that we attribute to a surface defect. This area was excluded from the region of interest used for the calculation of bulk H content in the sample. Chemical maps of the other samples showed no heterogeneities.

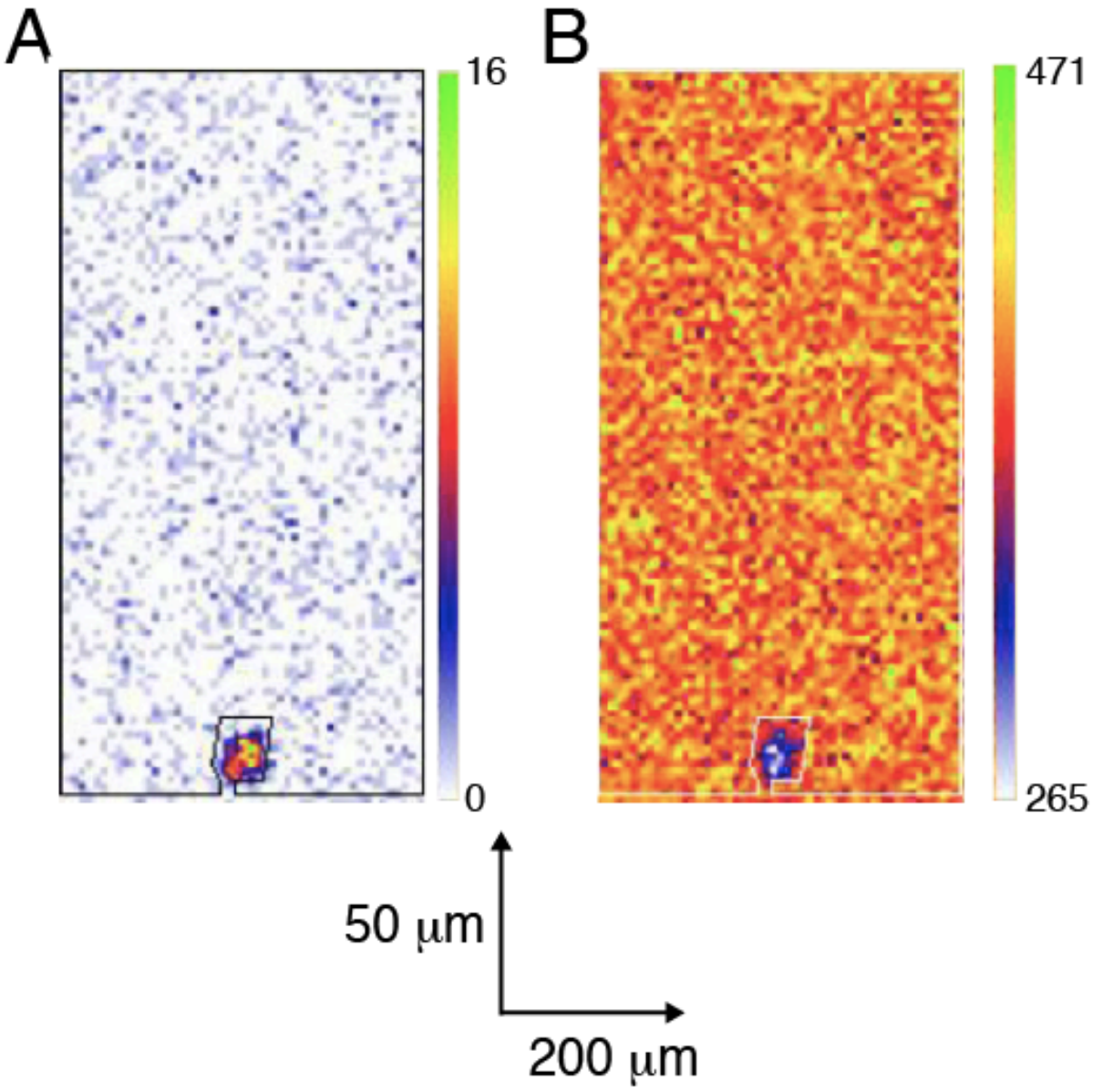

FIGURE OM6. Chemical maps of area of GRR771 measured by ERDA. Scales (in units corresponding to the sample surface) in the vertical and horizontal directions on the images are not equal, because the sample was inclined relative to the beam. Color scales to the right of each image are in units of cumulative detector counts. **a.** Bulk H map. The region of interest selected for quantification of bulk H is outlined in black. **b.** PIXE Ca map.

5. SIMS

Appendix Table OM3 (separate excel file) contains full SIMS data (cps, ratios, and uncertainties) from the 2012 and 2016 sessions.

Working curves for fluorine in the 2012 and 2016 sessions were established using F-bearing glasses (ML3B-G, KL2-G, BHVO-2G, BCR-2G, and/or Fba-1). $^{19}F/^{18}O$ data were blank corrected using either GRR332 or GRR1017. We use the following concentration values for F (in μg/g) derived by Mosenfelder et al. (2020): ML3B-G (63 ± 3); KL2-G (135 ± 4); BHVO-2G (307 ± 13); BCR-2G (366 ± 6); Fba-1 (1857 ± 92). The methodology for re-evaluating these reference values is described in the supplemental information to that paper. It should be emphasized that the homogeneity of the MPI-DING and USGS glasses for F has not been rigorously evaluated, and that the uncertainties may consequently be underestimated. Therefore, these concentrations are not necessarily recommended for use by other researchers using different sample splits of these reference materials.

The working curves for the two SIMS sessions are displayed in Figure OM7. The slopes of the York regressions fit to the data in 2012 and 2016 are identical within mutual uncertainties. The wide 95% confidence intervals (and high value for mean square weighted deviation, MSWD) for the 2012 data can be attributed to the small error bars assigned to the F reference values (within the symbol size on the graph in Fig. OM7a).

Figure OM8 displays two examples illustrating the cycle-to-cycle correlation between ^{16}OH and ^{19}F in individual analyses of JLM83a. This covariation indicates that zoning is coupled on a sub-micrometer scale, as discussed in the main text.

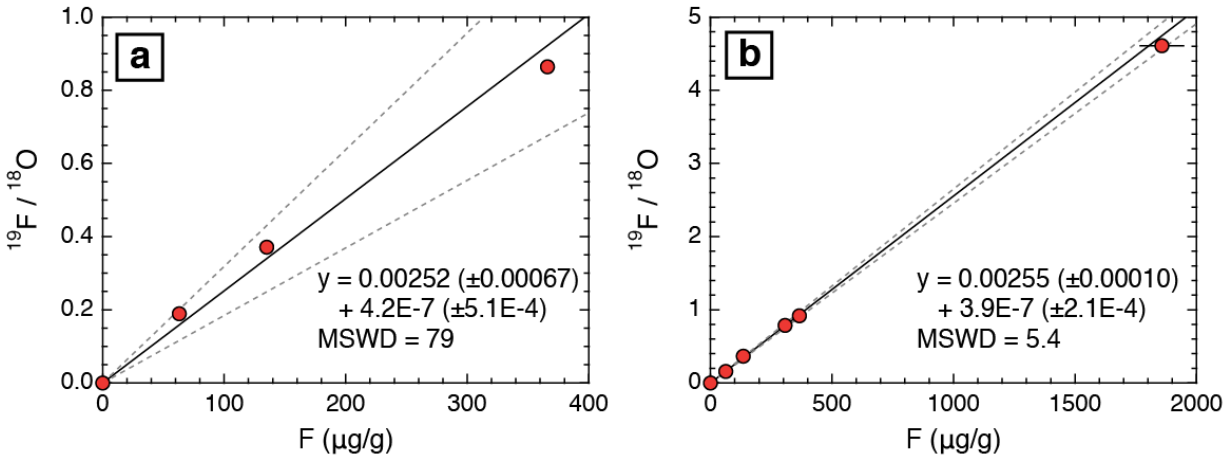

FIGURE OM7. SIMS working curves for F. Uncertainties (2*s*) not visible are within symbol size. York regressions for each dataset are plotted with lines labeled with respective equations and MSWD. 95% confidence intervals are shown with dashed lines. **a.** 2012 session. **b.** 2016 session.

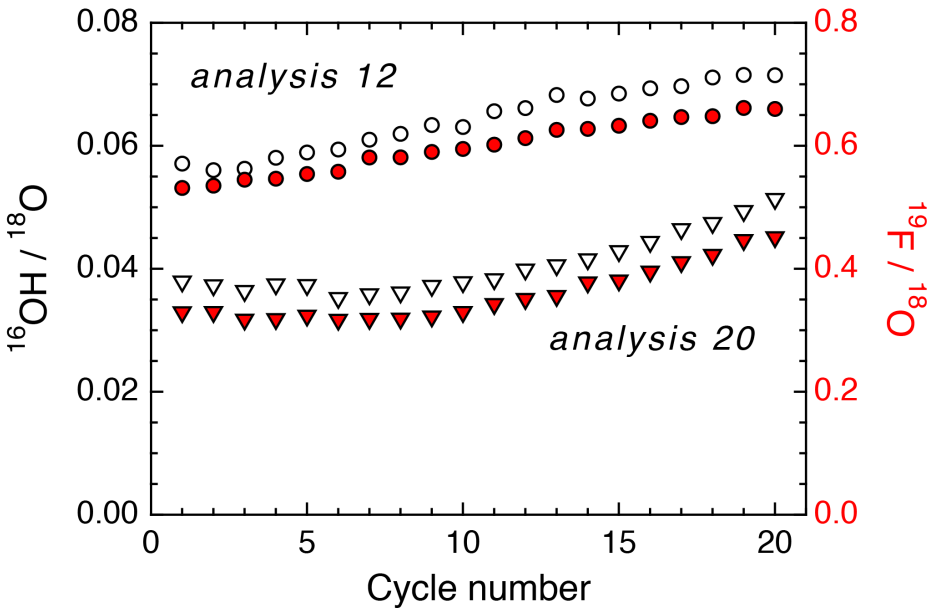

FIGURE OM8. Two analyses of JLM83a, demonstrating correlation between ^{16}OH and ^{19}F on a sub-micron scale. Open symbols are $^{16}OH/^{18}O$ values (left axis); closed symbols (red) are $^{19}F/^{18}O$ (right axis). Each analysis consists of 20 cycles through the mass sequence following pre-sputtering and automated alignment. Depth was not calibrated but is less than two microns total for each sputtered crater. Corresponding $s_{\bar{x}}/\hat{s}_{\bar{x}}$ values for analysis 12 (circles) are 7.9 for $^{16}OH/^{18}O$ and 12.2 for $^{19}F/^{18}O$; for analysis 20 (triangles) they are 9.3 for $^{16}OH/^{18}O$ and 18.1 for $^{19}F/^{18}O$.

6. EPMA

Figure OM9 is a comparison of F concentrations determined by EPMA and SIMS, as discussed in the main text. Figure OM10 summarizes the results of 132 EPMA analyses on JLM83a.

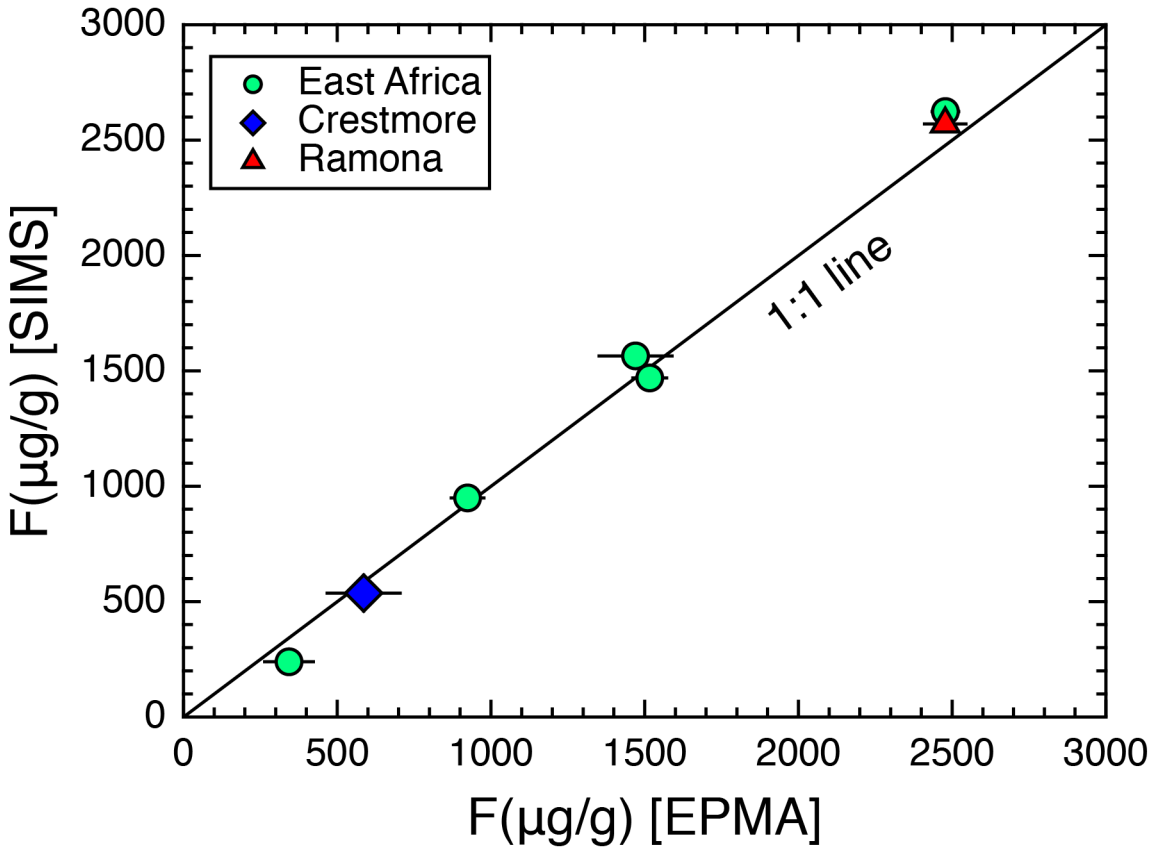

FIGURE OM9. Comparison of F concentrations determined from EPMA and the 2016 SIMS session, with 1:1 correspondence drawn as a solid line. Error bars reflect $2s_x$ uncertainties for 5 to 6 separate EPMA analyses. Only samples measured both by EPMA and during the 2016 SIMS session are displayed. GRR1429 (Essex) and GRR732 are excluded from this plot because F was not measured in either sample by EPMA, nor was either sample measured in the 2016 session. Substituting values determined by SIMS during the 2012 session yields a similar plot.

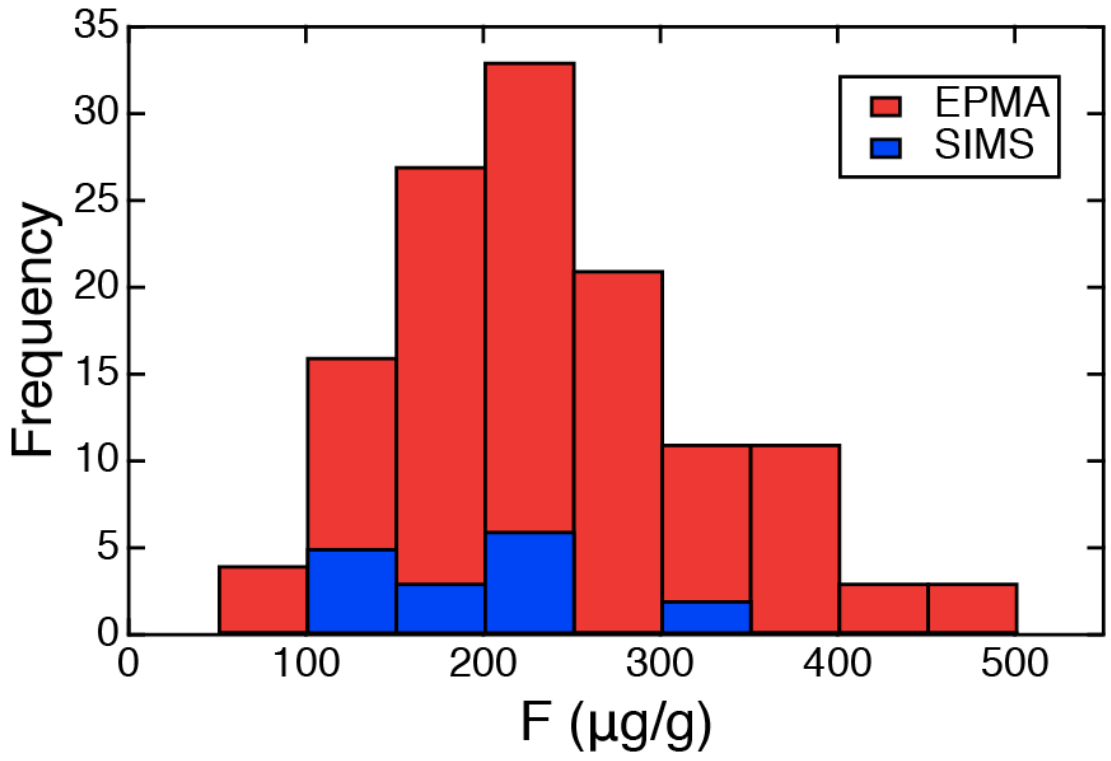

FIGURE OM10. Histogram of F concentrations measured in JLM83a by EPMA and SIMS. The EPMA analyses (n = 129) have a positively skewed distribution with an average of 237 ± 88 µg/g F (1s_x). Three analyses with F under the detection limit (40-60 µg/g F, depending on beam current) are not included in this graph.

7. Hydrous inclusions in grossular?

The assignment by Geiger and Rossman (2020a,b) of bands at 3674 and 3688 cm^{-1} to inclusions of serpentine (their preference) or other hydrous minerals is an attractive way to explain the presence of these high frequency bands in Asbestos grossular, which is derived from rodingites in a serpentinized ultramafic body. However, several lines of evidence contradict this hypothesis. First, the geologic setting of the Asbestos samples is unlike that of any of the other garnets in this study or in the literature that also have these absorption bands. These other garnets are associated with metamorphic rocks that have no serpentine (or talc) in their assemblage: the East African samples are mined or derived (as stream gravel) from veins and pockets in graphitic

gneisses associated with marble (Key and Hill 1989; Giuliani et al. 2008, 2011); the Crestmore (GRR1122) and Ramona (GRR42) garnets come from calcite skarn localities; and Essex County grossular (GRR1429; possibly from the Willsboro Mine, pers. comm. from John Valley) most likely formed by retrogression of high-*T* calc-silicate rocks in the Adirondack massif (Valley et al. 1983). The same bands (along with other high-frequency peaks) are also present in grossular-andradite garnets from skarn deposits in Thailand (Phichaikamjornwut et al. 2012). Parenthetically, we note that the F-rich environments were already established for grossular-bearing calc-silicate rocks from the Adirondacks (Valley et al. 1983) and gneisses from the Merelani Hills in Tanzania. The latter contain vanadian phlogopite with up to 2 wt% F (Giuliani et al. 2008).

Second, the band intensities scale with F content in the East African grossular garnets (Fig. OM1), and there is no evidence of spatial zoning in their intensities. O-H zoning might not be expected for hydrous inclusions formed by exsolution from the host (e.g., titanoclinohumite lamellae in olivine; Kitamura et al. 1987). However, serpentine minerals have no reaction relationship with grossular so their presence would require overgrowth of the garnet or deposition along fractures. Neither of these events are likely to result in homogeneously distributed hydrous inclusions.

Third, the symmetric structure of the band at 3688 cm^{-1} is unlike the signature of serpentine inclusions in olivine (Miller et al. 1987; Matsyuk et al. 2004) or ultramafic-hosted andradite, which sometimes contains optically visible "horsetail" inclusions of serpentine (most notably in demantoids from the Ural Mountains in Russia, but also in GRR1263 from San Benito County, CA, displayed in Figure 1 of Amthauer and Rossman 1989). In both cases, the O-H vibrations comprise three overlapping bands. Miller et al. (1987) described the bands assigned to

serpentine in olivine as being centered at 3645, 3685, and 3709 cm^{-1}, and Matsyuk et al. (2004) documented variation in these positions but presented spectra with similar band structures. As a further example, we fit the absorption from serpentine horsetail inclusions in an andradite from the Urals (GIA62952) with three bands centered at 3648, 3691, and 3700 cm^{-1}.

Finally, a band at 3688 cm^{-1} is clearly evident in the spectrum of nominally pure grossular synthesized at 800 °C and 0.2 GPa by Geiger and Armbruster (1997) and is included in the curve fit of the same spectrum provided by Geiger and Rossman (2020a). There is no reason to expect serpentine to form well outside of its stability field (e.g., Wegner and Ernst, 1983) within a matrix of completely different composition. It seems rather more likely that the synthesis experiment was contaminated with trace amounts of F, which may be a common, seldom recognized phenomenon in high *P-T* experiments (Mosenfelder et al., 2020). Coupled H-F substitution via F contamination might also explain some of the sharp high-frequency bands in synthetic pyrope. P-27, synthesized by Geiger et al. (1991), has bands at 3641, 3651, and 3665 cm^{-1} while Ti-bearing pyrope crystals synthesized by Khomenko et al. (1994) and Geiger et al. (2000) have a sharp band between 3681 and 3686 cm^{-1}. The presence of clumped OH-F defects could largely explain the differences between spectra of grossular crystals synthesized by Geiger and Armbruster (1997) and Withers et al (1998) (Fig. 1c).

REFERENCES

Allen, F.M., and Buseck, P.R. (1988) XRD, FTIR, and TEM studies of optically anisotropic grossular garnets. American Mineralogist, 73, 568-584.

Amthauer, G., and Rossman, G.R. (1998) The hydrous component in andradite garnet. American Mineralogist, 83, 835–840.

Arredondo, E.H., Rossman, G.R., and Lumpkin, G.R. (2001) Hydrogen in spessartine-almandine garnets as a tracer of granitic pegmatite evolution. American Mineralogist, 86, 485-490.

Aubaud, C., Withers, A.C., Hirschmann, M., Guan, Y., Leshin, L.A., Mackwell, S., and Bell, D.R. (2007) Intercalibration of FTIR and SIMS for hydrogen measurements in glasses and nominally anhydrous minerals. American Mineralogist, 92, 811-828.

Bureau, H., Raepsaet, C., Khodja, H., Carraro, A., and Aubaud, C. (2009) Determination of hydrogen content in geological samples using elastic recoil detection analysis (ERDA). Geochimica et Cosmochimica Acta 73, 3311–3322.

Cho, H., and Rossman, G.R. (1993) Single-crystal NMR studies of low-concentration hydrous species in minerals: grossular garnet. American Mineralogist, 78, 1149-1164.

Daudin, L., Khodja, H., and Gallien, J. P. (2003). Development of “position-charge-time” tagged spectrometry for ion beam microanalysis. Nuclear Instruments and Methods in Physics Research, B 210, 153-158.

Geiger, C.A., and Armbruster, T. (1997) $Mn_3Al_2Si_3O_{12}$ spessartine and $Ca_3Al_2Si_3O_{12}$ grossular garnet: dynamical structural and thermodynamic properties. American Mineralogist, 82, 740–747.

Geiger, C.A., and Rossman, G.R. (2020a) Micro- and nano-size hydrogarnet clusters and proton ordering in calcium silicate garnet: Part I. The quest to understand the nature of “water” in garnet continues. American Mineralogist, 105, 455-467.

Geiger, C.A., and Rossman, G.R. (2020b) Micro- and nano-size hydrogarnet clusters in calcium silicate garnet: Part II. Mineralogical, petrological, and geochemical aspects. American Mineralogist, 105, 468-478.

Geiger, C.A., Langer, K., Bell, D.R., Rossman, G.R., and Winkler, B. (1991) The hydroxide component in synthetic pyrope. American Mineralogist, 76, 49–59.

Geiger, C.A., Stahl, A., and Rossman, G.R. (2000) Single-crystal IR- and UV/ VIS-spectroscopic measurements on transition-metal-bearing pyrope: The incorporation of hydroxide in garnet. European Journal of Mineralogy, 12, 259–271.

Giuliani, G., Ohnenstetter, D., Palhol, F., Feneyrol, J., Boutroy, E., de Boissezon, H., and Lhomme, T. (2008) Karelianite and vanadian phlogopite from the Merelani Hills gem zoisite deposits, Tanzania. Canadian Mineralogist, 46, 1183-1194.

Giuliani, G., Fallick, A.E., Feneyrol, J., Ohnenstetter, D., Pardieu, V., and Saul, M. (2011) $^{18}O/^{16}O$ and V/Cr ratios in gem tsavorites from the Neoproterozoic Mozambique metamorphic belt: a clue towards their origins? Mineralium Deposita, 46, 671-676.

Jenkins, W.O. (1943) Tungsten deposits northeast of Visalia, California. California Journal of Mines and Geology, 39, 169-182.

Key, R.M., and Hill, P.G. (1989) Further evidence for the controls on the growth of vanadium grossular garnets in Kenya. Journal of Gemmology, 21, 412-422.

Khodja, H., Berthoumieux, E., Daudin, L., and Gallien, J.P. (2001) The Pierre Sue Laboratory nuclear microprobe as a multi-disciplinary analysis tool. Nuclear Instruments and Methods in Physics Research Section B: Beam Interactions with Materials and Atoms 181, 83–86.

Khomenko, V.M., Langer, K., Beran, A., Koch-Müller, M., and Fehr, T. (1994) Titanium substitution and OH-bearing defects in hydrothermally grown pyrope crystals. Physics and Chemistry of Minerals, 20, 483-488.

Kitamura, M., Kondoh, S., Morimoto, N., Miller, G.H., Rossman, G.R., and Putnis, A. (1987) Planar OH-bearing defects in mantle olivine. Nature, 328, 143-145.

Koga, K., Hauri, E., Hirschmann, M.M., and Bell, D. (2003) Hydrogen concentration analyses using SIMS and FTIR: comparison and calibration for nominally anhydrous minerals. Geochemistry, Geophysics, and Geosystems, 4, doi: 10.1029/2002GC000378.

Matsyuk, S.S., and Langer, K. (2004) Hydroxyl in olivines from mantle xenoliths in kimberlites from the Siberian platform. Contributions to Mineralogy and Petrology, 147, 413–437.

Mayer, M. (1999). SIMNRA, a simulation program for the analysis of NRA, RBS, and ERDA. Proceedings of the 15th International Conference on the Application of Accelerators in Research and Industry, 475, 541-544.

Miller, G.H., Rossman, G.R., and Harlow, G.E. (1987) The natural occurrence of hydroxide in olivine. Physics and Chemistry of Minerals, 14, 461–472.

Mosenfelder, J.L., Le Voyer, M., Rossman, G.R., Guan, Y., Bell, D.R., Asimow, P.D., and Eiler, J.M. (2011) Analysis of hydrogen in olivine by SIMS: evaluation of standards and protocol. American Mineralogist, 96, 1725-1741.

Mosenfelder, J.L., Rossman, G.R., and Johnson, E.A. (2015) Hydrous species in feldspars: a reassessment based on FTIR and SIMS. American Mineralogist, 100, 1209-1221.

Mosenfelder, J.L., Andrys, J.L., von der Handt, A., Kohlstedt, D.L., and Hirschmann, M.M. (2020) Hydrogen incorporation in plagioclase. Geochimica et Cosmochimica Acta, 277, 87–110.

O'Leary, J.A., Rossman, G.R., and Eiler, J.M. (2007) Hydrogen analysis in minerals by continous-flow mass spectrometry. American Mineralogist, 92, 1990-1997.

Phichaikamjornwut, B., Skogby, H., Ounchanum, P., Limtrakun, P., and Boonsoong, A. (2012) Hydrous components of grossular-andradite garnets from Thailand: thermal stability and exchange kinetics. European Journal of Mineralogy, 24, 107-121.

Raepsaet, C., Bureau, H., Khodja, H., Aubaud, C., and Carraro, A. (2008) μ-ERDA developments in order to improve the water content determination in hydrous and nominally anhydrous mantle phases. Nuclear Instruments and Methods in Physics Research Section B: Beam Interactions with Materials and Atoms 266, 1333–1337.

Rossman, G.R., and Aines, R.D. (1986) Spectroscopy of birefringent grossular from Asbestos, Quebec, Canada. American Mineralogist, 71, 779-780.

Rossman, G.R., and Aines, R.D. (1991) The hydrous components in garnets: grossular-hydrogrossular. American Mineralogist, 76, 1153-1164.

Rossman, G.R., Rauch, F., Livi, R., Tombrello, T.A., Shi, C.R., and Zhou, C.Y. (1988) Nuclear reaction analysis of hydrogen in almandine, pyrope, and spessartite garnets. Neues Jahrbuch für Mineralogie Monatshefte, H.4, 172-178.

Valley, J.W., Essene, E.J., and Peacor, D.R. (1983) Fluorine-bearing garnets in Adirondack calc-silicates. American Mineralogist, 68, 444-448.

van Roermund, H.L.M., Drury, M.R., Barnhoorn, A., and de Ronde, A.A. (2000) Super-silicic garnet microstructures from an orogenic garnet peridotite, evidence for an ultra-deep (>6 GPa) origin. Journal of Metamorphic Geology, 18, 135-147.

Wegner, W. W., and Ernst, W. G. (1983) Experimentally determined hydration and dehydration reactions in the system $MgO–SiO_2–H_2O$. American Journal of Science, 283-A, 151–180.

Withers, A.C., Wood, B.J., and Carroll, M.R. (1998) The OH content of pyrope at high pressure. Chemical Geology, 147, 161-171.

Withers, A.C., Bureau, H., Raepsaet, C., and Hirschmann, M.M. (2012) Calibration of infrared spectroscopy by elastic recoil detection analysis of H in synthetic olivine. Chemical Geology, 334, 92-98.